

Mar.2022 / Vol.177

M i t s u b i s h i E l e c t r i c

ADVANCE

High-frequency and Optical Devices

- **Editorial-Chief**

Hideyuki Ichiyama

- **Editorial Advisors**

Masayuki Sato
Hisao Takahashi
Omi Kuriwaki
Yukiko Funada
Tomohito Nakata
Kiyofumi Takeuchi
Tetsuo Kojima
Makoto Sato
Takao Ikai
Hiroshi Usui
Satoru Yamaguchi
Hideya Tadokoro
Eunjin Choi
Kazuki Yamanaka
Yuichiro Arata
Toshihiro Kurita

- **Vol. 177 Feature Articles Editor**

Eitaro Ishimura

- **Editorial Inquiries**

Hideyuki Ichiyama
Corporate Productivity Engineering &
Logistics Dept.
Fax: +81-3-3218-2465

Mitsubishi Electric Advance is published on line quarterly (in March, June, September, and December) by Mitsubishi Electric Corporation. Copyright © 2022 by Mitsubishi Electric Corporation; all rights reserved. Printed in Japan.

The company names and product names described herein are the trademarks or registered trademarks of the respective companies.

CONTENTS

Overview1
by Masayoshi Takemi

Technical Reports

GaN HEMT Supporting Multi-Carrier Communications for Ku-band
Satellite Communication Systems2
by Takumi Sugitani and Takashi Yamasaki

High-power 10-Gbps EML CAN for Combo-PON5
by Yu Uwadori and Takashi Nagira

50-Gbps EML CAN for 5G Base Stations8
by Yojiro Watanabe and Hayata Fukushima

100-Gbps EML CAN for 5G Mobile Communication System11
by Seiji Nakano and Masaki Nasu

80×60 Pixels Thermal Diode Infrared Sensor14
by Yoshinori Takahashi and Tomohiro Maegawa

Shortening of Evaluation Time by Highly Accelerated Stress Test
and Improvement of Analysis Technique for Passivation Film
.....17
by Koichi Inoue and Hajime Sasaki

Precis

Digital transformation (DX) is being promoted to reform products, services, and business models by using data and digital technologies, making information communication and sensor technologies increasingly important. This issue introduces the latest high-frequency and optical devices for telecommunications, infrared sensors, and related technologies.

Overview



Author: *Masayoshi Takemi**

The Latest Trends and Future Outlook of High Frequency and Optical Devices

Digital transformation (DX) is becoming increasingly important in various ways, including for suppressing COVID-19 by helping to shift to economic activities with less physical contact with other people and new lifestyles. DX requires the fifth generation mobile communication system (5G), Internet of Things (IoT) using 5G infrastructure, and optical communication networks for transmitting large volumes of data. 5G uses technologies including enhanced mobile broadband (eMBB), ultra-reliable and low latency communications (URLLC), and massive machine type communications (mMTC). Base stations having antennas with massive multi-input multi-output (massive MIMO) are being constructed and many of these antennas emit radio waves whose phases and amplitudes are controlled. The transmission of such radio waves to many users concurrently achieves both mMTC and high-speed large-capacity communications. Mitsubishi Electric Corporation has developed and commercialized small low-heat high-efficiency gallium nitride (GaN) amplifiers for this application. In addition, optical communication networks are the core of communication infrastructure; in order to cope with greater total communication traffic volume with the spread of larger data centers, cloud services and the Internet in addition to 5G, the speed and transmission capacity of all layers of the network have been enhanced. We have achieved operation at 25 gigabits per second (Gbps) for distributed feedback laser diodes (DFB-LDs) and 100 Gbps for electro-absorption modulated lasers (EMLs). Furthermore, we have commercialized small high-performance, low-cost infrared sensor modules, MeDIR. These modules reduce costs and increase the number of pixels, and are expected to be used for the IoT.

GaN HEMT Supporting Multi-Carrier Communications for Ku-band Satellite Communication Systems

Authors: Takumi Sugitani* and Takashi Yamasaki*

Increasing information transmission capacity and speed is currently driving strong demand for Ku-band multi-carrier satellite communications. Low distortion characteristics (third-order intermodulation distortion, IM3, -25dBc or less) at wide offset frequencies are required for GaN power amplifiers, accordingly. With a newly developed matching circuit, the two GaN HEMTs introduced here achieve a low measured IM3 of less than -25 dBc at the maximum offset frequency (Δf) of 400 MHz while delivering a peak output power of approximately 70 W or 30 W.

1. Introduction

In recent years, gallium nitride (GaN) high electron mobility transistor (HEMT) power amplifiers have been increasingly used in transmitters for satellite communications. Mitsubishi Electric Corporation has been commercializing a Ku-band 70-W GaN HEMT (MGFK48G3745) as power amplifiers for single-carrier satellite communication earth stations.⁽¹⁾⁽²⁾ The current demand for further increase in the information transmission capacity and speed strongly requires GaN HEMT power amplifiers that can support multi-carrier communications. In such multi-carrier communications, it is very important to maintain low IM3 over a wide Δf range as well as to transmit high peak output power. This paper reports on two different power-classes (70 W and 30 W) of GaN HEMTs suitable for Ku-band multi-carrier satellite communications. The matching circuit featuring three different types of difference-frequency short circuits allows the GaN HEMTs to deliver a low IM3 of less than -25 dBc over a wide Δf range of up to 400 MHz.⁽³⁾

2. Ku-band 70-W GaN HEMTs for Multi-carrier Communications

Figure 1 illustrates the simplified schematic of the conventional output matching circuit used in a GaN HEMT (MGFK48G3745). For the conventional circuits, the resonance frequency in the low frequency band is set to approximately 5 MHz by the single short circuit placed near the drain bias circuit outside the package. Figure 2(a) shows the simulated impedance of the output matching circuit seen from the drain terminals of the FETs. Figure 2(b)

shows the measured offset frequency (Δf) dependence of the IM3 for the above GaN HEMT under 14.125-GHz-band two-tone tests.

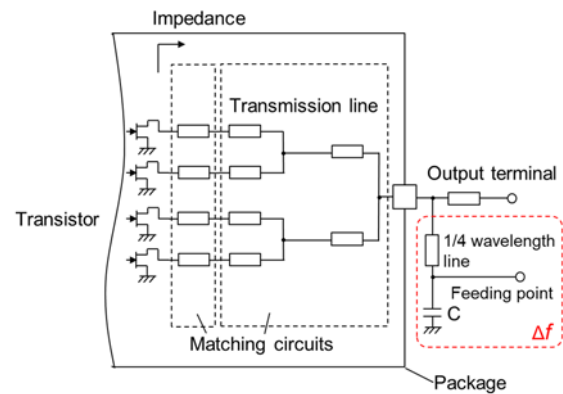
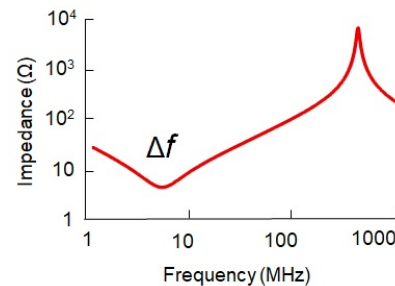
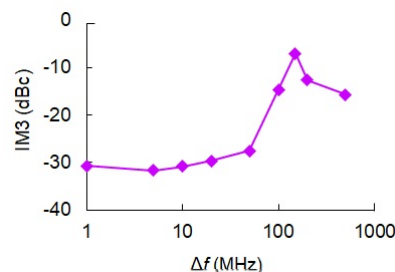


Fig. 1 Simplified schematic of conventional output matching circuit



(a) Simulated impedance looking into the conventional output matching circuit from all the drain terminals



(b) Measured Δf dependence of IM3 characteristics for the conventional output matching circuit

Fig. 2 Simulated impedance looking into the conventional output matching network from all the drain terminals and measured Δf dependence of IM3 characteristics for the conventional output matching circuit

In the figure, Δf is the difference in the frequencies of two tones and the output power level per tone was 40 dBm. To realize low IM3 over a wide Δf of up to 400 MHz, we have adopted the output matching circuit shown in Fig. 3. The circuit features three different types of difference-frequency short circuits; two of which are embedded into a tournament-shaped output matching circuit inside the package and the rest is embedded into the drain bias feed placed outside the package. On the basis of our original analysis, the following three resonance frequencies were determined to be $\Delta f_1 = 157$ MHz, $\Delta f_2 = 27$ MHz, and $\Delta f_3 = 5$ MHz.⁽³⁾

Figure 4 shows the inside micrograph of a Ku-band 70-W GaN HEMT (MGFK48G3745A) for multi-carrier communications. The difference-frequency short circuits use $\lambda/4$ lines and several nF wire-bonding-mount-type microchip capacitors. These circuits are deployed not only in the output matching circuit, but also in the input matching one to suppress the imbalance between the upper and lower IMD3.

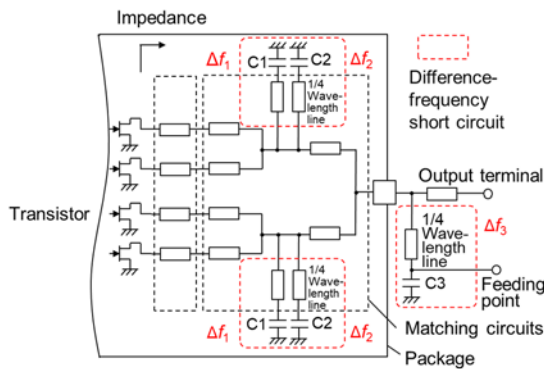


Fig. 3 Simplified schematic of output matching circuit supporting multi-carrier communications

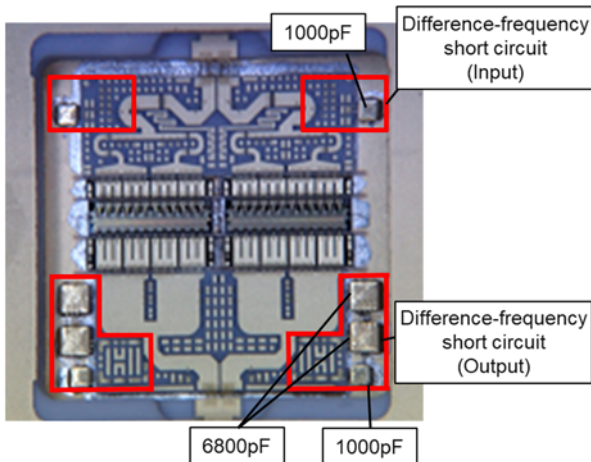
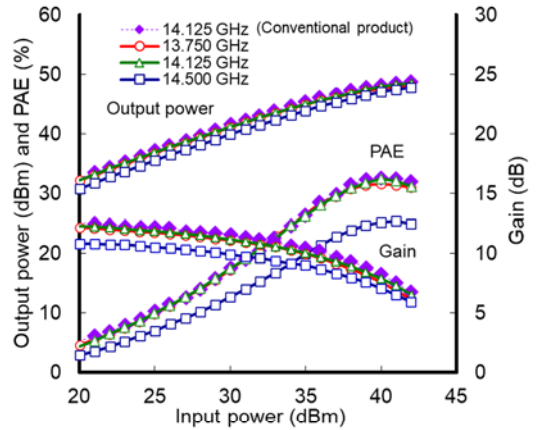
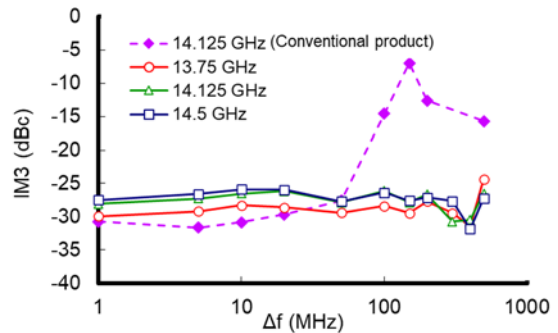


Fig. 4 Ku-band 70-W GaN HEMT (MGFK48G3745A) supporting multi-carrier communications



(a) Measured output power transfer characteristics



(b) Measured dependence of IM3 on Δf for the 70-W GaN-HEMT

Fig. 5 RF and Δf dependence of IM3 characteristics of Ku-band 70-W GaN HEMT supporting multi-carrier communications

Figures 5(a) and (b) show the measured output power transfer characteristics and the measured dependence of IM3 on Δf for the 70-W GaN-HEMT, respectively, under a 24-V drain voltage and a single-tone CW signal condition, where the measurement frequencies are at 13.75, 14.125, and 14.5 GHz. Figure 5 also compares the characteristics with and without difference-frequency short circuits. As can be seen in the figures, the 70-W PA achieves a peak output power of 48.6 dBm (72.4 W) at 14.125 GHz while maintaining a linear output power of over 40 dBm and an IM3 of -26 dBc. Over the frequency range from 1 MHz to 400 MHz, IM3 is successfully suppressed to less than -26 dBc. Thus, while maintaining the low IM3 required for multi-carrier communications, the 70-W GaN HEMT achieves high output and high gain characteristics similar to those of the conventional single carrier GaN HEMT product.

3. Ku-band 30-W GaN HEMTs for Multi-Carrier Communications

Regarding the output power levels of power amplifiers for satellite communications, there is a demand not only for higher-power products, but also for relatively low-power products. This is because for small earth stations, products with various output power

specifications are commercially used depending on the size and cost of the stations. This time, we have also developed a Ku-band 30-W GaN HEMT (MGFK45G3745A) for multi-carrier communications to address the need for relatively low-power products. Regarding the package, the same packages as those of the Ku-band 70-W GaN HEMTs were used considering the compatibility. Inside the package, only one GaN HEMT chip is used; the chip is the same that as used for the 70-W GaN-HEMT (Fig. 4). The matching circuit design for the 30-W GaN-HEMT was the same as that previously described for the 70-W GaN-HEMT.

The measured output power transfer characteristics and the measured dependence of IM3 on Δf for the 70-W GaN-HEMT are shown in Figs. 6(a) and (b), respectively, under a 24-V drain voltage and a single-tone CW signal condition. A peak output power of approximately 46.0 dBm and a linear gain of higher than 10.8 dB are achieved at 14.125 GHz. Over the same frequency band, the PA offers a peak output power larger than 45.2 dBm and a linear gain of over 10.0 dB. Figure 6(b) shows the IM3 characteristics at a single-carrier output power level of 36.3 dBm, indicating that an IM3 of less than -26 dBc is

well suppressed at offset frequencies from 1 MHz up to 500 MHz. The measurements reveal that the 70-W GaN HEMT achieves high output and high gain characteristics while the low IM3 required for multi-carrier communications is maintained.

4. Conclusion

Regarding the use of power amplifiers for Ku-band satellite communication earth stations, we have commercialized Ku-band 70-W GaN HEMTs (MGFK48G3745A) supporting multi-carrier communications with Δf of 400 MHz and Ku-band 30-W GaN HEMTs (MGFK45G3745A), which is a lower output model similar to the 70-W GaN HEMTs. These HEMTs feature our original, low-distortion matching circuit design. The package size is the same as that of packages for the already commercialized 70-W GaN HEMTs (MGFK48G3745). The addition of these Ku-band GaN HEMT products to our lineup will help reduce the size of satellite communication earth stations and increase the information transmission capacity and speed.

Acknowledgement

These results were obtained in research conducted under a contract with the New Energy and Industrial Technology Development Organization (NEDO) of Japan.

References

- (1) Tetsuo K., et al.: High Gain and High Power Internally Matched GaN HEMT for Ku-band Satellite Communications, *Mitsubishi Denki Giho*, 91, No. 5, 293–296 (2017)
- (2) Hiroaki M., et al.: Ku-Band GaN HEMT Amplifier with 100W Output Power, *Mitsubishi Denki Giho*, 87, No. 2, 113–115 (2013)
- (3) Yoshioka, T., et al.: A Ku-band 70-W Class GaN Internally Matched High Power Amplifier with Wide Offset Frequencies of up to 400 MHz for Multi-Carrier Satellite Communications, 2020 IEEE BICMOS and Compound Semiconductor Integrated Circuits and Technology Symposium, BCICTS (2020)

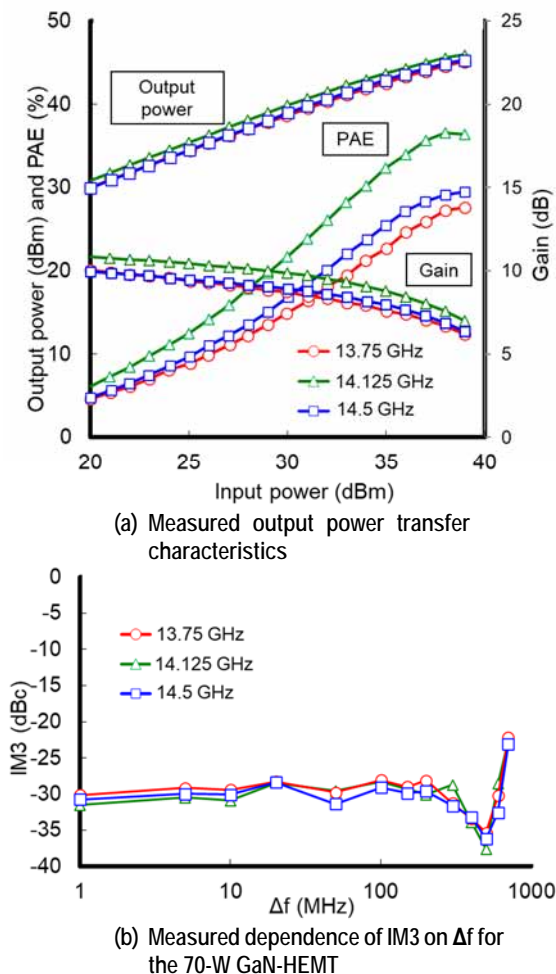


Fig. 6 RF and Δf dependence of IM3 characteristics of Ku-band 30-W GaN HEMT supporting multi-carrier communications

High-power 10-Gbps EML CAN for Combo-PON

Authors: Yu Uwadoi* and Takashi Nagira*

For Fiber To The Home (FTTH) systems, Combo-PON, which is compatible with 1-Gbps and 10-Gbps passive optical networks (PONs), has been spreading. For Combo-PON, there is demand for higher-power 10-Gbps electro-absorption modulated lasers (EMLs). In this development, the structure of EML elements was optimized to realize CAN EMLs that satisfy the Combo-PON (D1) standard.

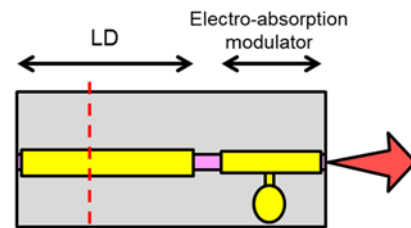
injection into the active layer of the laser diode, the active layer was buried within Indium phosphide (InP) to form a current blocking layer. In addition, a buried structure improves thermal dissipation around the current injection path. These improvements increased the optical output efficiency; the optical output when the LD current (I_{op}) was 109 mA, which is a typical driving condition, was increased by 1.2 dB to 11.7 dBm.

1. Introduction

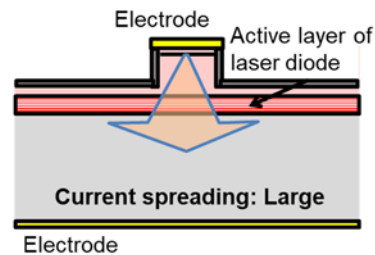
In a PON system, a single optical fiber connected to the optical line terminal (OLT) is branched out using a photocoupler and the branched lines are connected to multiple optical network units (ONUs). Currently, Gigabit-PON (G-PON) is being upgraded to 10-gigabit symmetric-PON (XGS-PON). However, both G-PON and XGS-PON are used on the end user side and so the structure needs to be designed to support both types. Under such circumstances, Combo-PON involving optical transceivers that are compatible with both G-PON and XGS-PON has been spreading. Because multiplexing of G-PON/XGS-PON is performed in optical transceivers for Combo-PON, the optical system tends to be complicated, which increases the optical loss. Accordingly, there is demand for higher-power CAN EMLs that are expected to be used as light sources for 10-Gbps systems. In this study, we reviewed the design of EML elements in detail to increase the optical output and improve the fiber coupling efficiency by narrowing the beam angle.

2. Higher Power Achieved by Changing the Element Structure

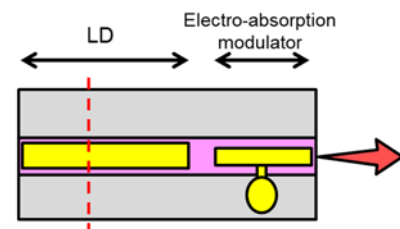
The conventional ridge-type EML element (Figs. 1(a) and 1(b)) cannot satisfy the needs for high optical output, high fiber coupling efficiency, and low power consumption that are demanded in Combo-PON. Accordingly, we have developed a new EML element that can satisfy such needs and has a high yield rate. To meet the Combo-PON (D1) standard, the optical output (PL) through the lens needs to be increased to 11 dBm from the conventional 9.5 dBm. To achieve this, the structure of the EML element was changed to the buried type (Figs. 1(c) and 1(d)) from the ridge type. To improve the efficiency of the current



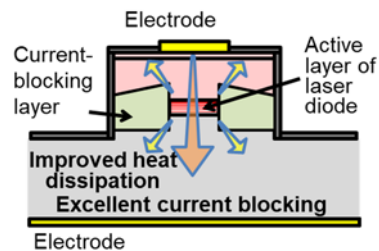
(a) Top view of ridge type



(b) Cross section of ridge type



(c) Top view of buried type

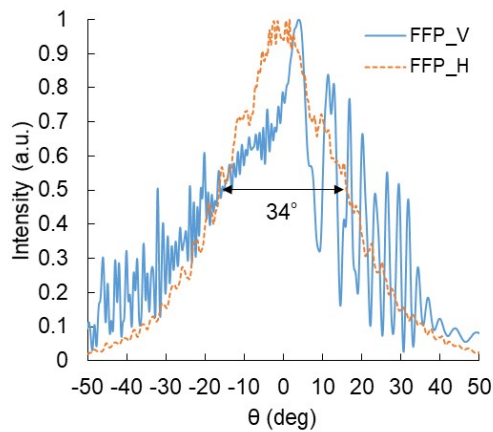


(d) Cross section of buried type

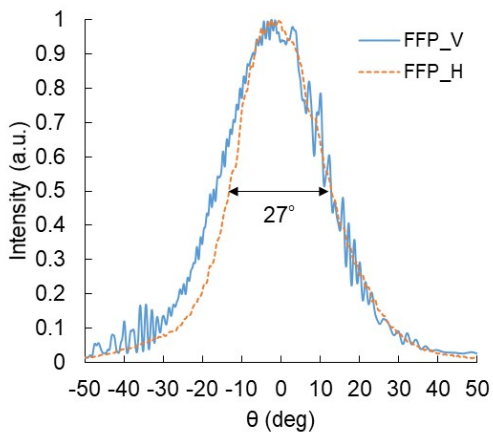
Fig. 1 Schematic structure of EML

3. Narrower Beam Angle Realized by Changing the Element Structure

The shape of generated beams is determined based on the matching of the waveguide mode between the LD (light source) and the electro-absorption modulator (EAM, light-emitting side), as well as the shape of the waveguide mode of the EAM. The structure of the EAM was also changed to the buried type from the conventional ridge type as is the case with the structure of the LD to match the waveguide modes of the LD(1), and the angle of the generated beams was narrowed. This reduced ripples in the vertical beam shape (FFP-V) caused by mismatching of the waveguide modes between the LD and EAM. In addition, the diameter of the waveguide mode of the EAM was increased, which narrowed the beam emission angle from 34 degrees of the ridge type to 27 degrees (full width half maximum) (Fig. 2). As a result, the efficiency of fiber coupling to a single-mode fiber increased from 59% of the ridge type to 71%, and the output of the optical transceiver increased by 0.8 dB.



(a) Ridge type

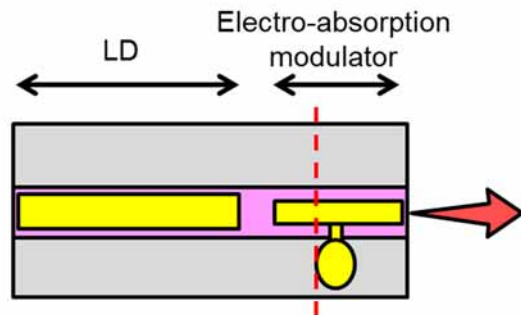


(b) Buried type

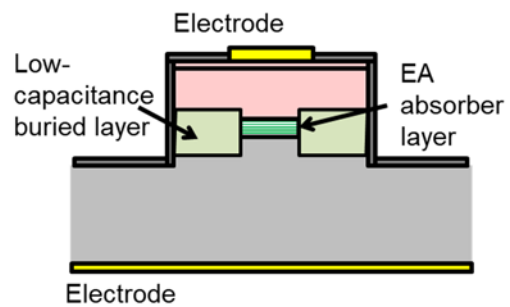
Fig. 2 Far field pattern

4. Stabilization of the High Frequency Characteristic

The application of the buried-type structure increased the optical output through the lens. However, it was found that the modulated optical waveform degraded because of insufficient high-frequency band, when the LD and EAM are buried within the same current blocking layer. These degraded waveforms are caused by an increase of capacitance, and we attributed the increase of capacitance to adoption of the same buried structure by the EAM as that of the LD.(2) To prevent this, we considered using a lower-capacitance structure for the buried layer (Fig. 3). However, it is necessary to match the waveguide mode between LD and EAM, when the structure of EAM is changed. Therefore, we developed the manufacturing process to remove a part of the current blocking layer from EAM. This developed process achieved a structure which reduces the capacitance, matching the waveguide mode. As a result, the lower-capacitance buried layer solved the problem of defective optical output waveforms and improved the mask margin (MM) from -20% to +30% or more.



(a) Top view of buried type



(b) Cross section of EAM

Fig. 3 Schematic structure of EAM

5. Evaluation Results of EML CAN

The EML element designed as described above was installed onto a CAN package to evaluate the frequency response characteristic and optical output waveforms. Figure 4 shows the evaluated frequency response characteristic. The frequency is 9 GHz in the 3-dB band as the pass characteristic and is the same as that of the product with the conventional ridge type element. Figure 5 shows the back-to-back (BTB) optical output waveforms. As the driving conditions, the bit rate was 10.3 Gbps, the case temperature (Tc) was 25°C, the EML set temperature (Tld) was 45°C, the LD driving current (Iop) was 109 mA, the EML's modulation voltage amplitude (Vpp) was 2 V, and the EA offset voltage (Voff) was -0.6 V. For the evaluation, a flexible printed circuit (FPC) was connected to the CAN package. The evaluation results showed excellent optical output waveforms, with an extinction ratio of 10 dB and mask margin of 25%.

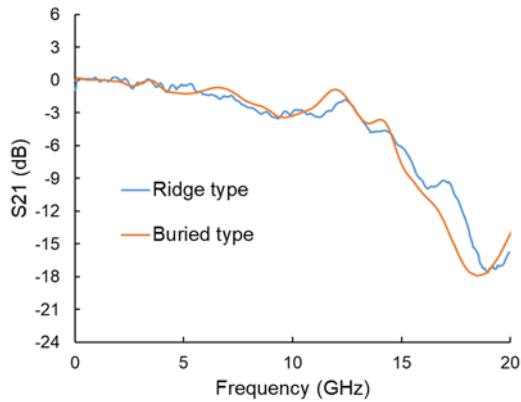


Fig. 4 Experimental results of frequency response

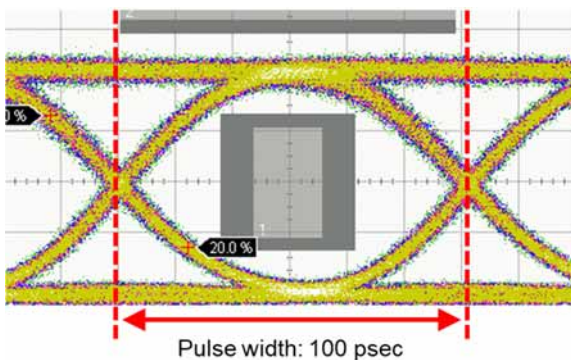


Fig. 5 10.3-Gbps eye diagram

6. Conclusion

We have developed a high-power 10-Gbps EML CAN for Combo-PON. The structure of the EML element was changed to the buried type, which improved the efficiency of the current injection to the active layer of the laser diode and heat dissipation. The optical output reached 11.7 dBm, which satisfies the Combo-PON (D1) standard of 11 dBm. The structure of the electro-absorption modulator was also changed to the buried type; while the waveguide modes were matched, the angle of generated beams was narrowed from 34 degrees to 27 degrees and the fiber coupling efficiency was improved by 0.8 dB. In addition, the structure of the electro-absorption modulator was changed to the buried type with lower capacitance, which eliminated defective optical output waveforms. The EML element was installed onto a CAN package. It was confirmed that the pass characteristic is the same as that of the ridge type and the obtained optical output waveforms were excellent, with an extinction ratio of 10 dB and mask margin of 25%.

References

- (1) P. M. Asbeck, et al.: Lateral mode behavior in narrow stripe lasers, *IEEE J. Quantum Electronics*, QE-15, 727 (1979)
- (2) N. H. Zhu, et al.: Electrical and Optical Coupling in an Electroabsorption Modulator Integrated with a DFB Laser, *IEEE J. Quantum Electronics*, 43, 535 (2007)

50-Gbps EML CAN for 5G Base Stations

Authors: Yojiro Watanabe* and Hayata Fukushima*

The fifth-generation mobile communication system (5G) is spreading to satisfy the need for larger transmission capacity driven by the rapid increase in data traffic. Accordingly, there is demand for electro-absorption modulated lasers (EMLs) that operate with 26-Gbaud 4-level pulse amplitude modulation (PAM4) as optical devices with the transmission speed of 50 Gbps to be applied to midhaul of 5G base station networks. In this study, we optimized the transmission line on the flexible printed circuit (FPC) of 25-Gbps EML CAN⁽¹⁾ and driving conditions. The obtained characteristics conformed to 50GBASE-ER (26-Gbaud PAM4, transmission distance of 40 km), which is a standard for midhaul of 5G base stations.

1. Introduction

In order to satisfy the need for larger transmission capacity, 5G is spreading. Large-capacity communication systems are used for the base stations where the traffic concentrates and higher-speed optical devices are applied to each layer. For midhaul, optical devices with the transmission speed of 50 Gbps are applied and the transmission distance is 40 km.

As a general method to realize the transmission speed of 50 Gbps, EML elements are installed onto box packages consisting of ceramic and metal and are operated with 26-Gbaud PAM4. When CAN packages are applied, band limiting occurs due to impedance mismatch, making it difficult to obtain sufficient band for operation with 26-Gbaud PAM4.

In the present study, we optimized the transmission line on the FPC of 25-Gbps EML CAN and driving conditions. In the case of operation with 26-Gbaud PAM4, the extinction ratio was 7.0 dB and the transmitter and dispersion eye closure quaternary (TDECQ) was 2.0 dB. The electric power consumption of the thermoelectric cooler was 0.19 W when the case temperature was +80°C and 0.20 W when it was -5°C. It could be reduced by 23% compared to 0.26 W for box packages. The low-cost low-power consumption CAN package that operates at C-temp (-5°C to +80°C) provides characteristics that satisfy midhaul standard 50GBASE-ER (extinction ratio ≥ 6 dB, TDECQ ≤ 3.2 dB).

2. External Shape of the Package

The outside diameter of a CAN package for 50-Gbps EML CAN is industry-standard 5.6 mm. The characteristics of EMLs greatly change as the

temperature changes and so a thermoelectric cooler and thermistor to detect the temperature near the EML are required to control the temperature of the EML at a certain level. In addition, in order to control the driving current of the laser diode, a photodiode to monitor the optical output from the EML back facet has been built in. The lens cap has the widely-used cylindrical shape.

3. Structure of the EML Element

At the laser section of the EML, a highly-efficient buried waveguide that functions well at high temperatures is used. For the electro-absorption (EA) modulator section, in order to realize low modulation voltage and high-speed operation, the size was extended and the width of the absorption layer was reduced. Because reducing the absorption layer width deteriorates the optical confinement factor, a high-mesa waveguide is used to retain a high factor.⁽²⁾ Thus, the structure of the waveguide at the laser section differs from that at the EA modulator section, which enhances the characteristics of both sections. In addition, a spot-size converter installed at the end of the EA modulator section improves the efficiency of fiber coupling to single-mode fibers.

4. Impedance of the Transmission Line on the FPC and Frequency Characteristics

Band deterioration of a CAN package is caused by impedance mismatch between the driver IC that drives the EML and the EML element. In particular, electrical multiple reflection that occurs between the stemmed glass penetration section and EML element often causes band deterioration. Therefore, the impedance matching was improved including the transmission line in the CAN package.⁽¹⁾ In addition, the impedance of part of the transmission line on the FPC was adjusted so that unevenness of the gain is compensated by reflected waves according to the impedance mismatch at the stemmed glass penetration section. Figure 1 shows a schematic diagram. At the impedance adjustment section, reflected waves are superposed based on the frequency, compensating the frequency response characteristics. Figure 2 shows the frequency response characteristics when the impedance values were changed at the same section of the transmission line on the FPC. The results show that the provided impedance adjustment section can smooth the frequency response characteristics.

5. Evaluation Results

Based on the results in Section 4, the transmission line on the FPC was optimized. As a result, the 3-dB cut-off frequency of the frequency response characteristics of the 50-Gbps EML CAN including the transmission line (e.g., on the FPC) was 19.4 GHz. Figure 3 shows the back-to-back optical waveforms. As the driving conditions, the case temperature (T_c) was 25°C, the

EML set temperature (T_{ld}) was 50°C, the LD driving current (I_{op}) was 100 mA, the modulation voltage swing of EA (V_{pp}) was 1.3 V, and the bias voltage of EA (V_{off}) was -1.5 V. As the evaluation results, the extinction ratio was 7.0 dB and TDECQ was 2.0 dB. Thus, the obtained characteristics conform to midhaul standard 50GBASE-ER.

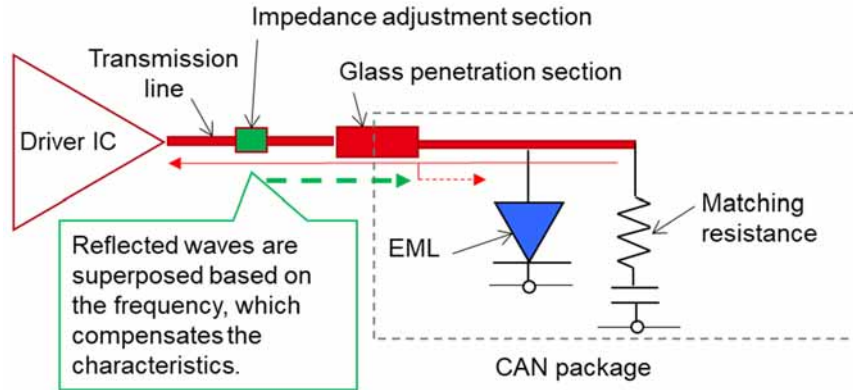


Fig. 1 Impedance adjustment compensating frequency response

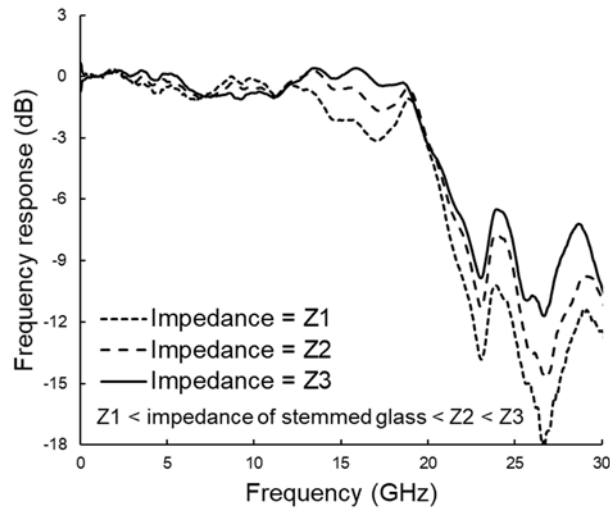


Fig. 2 Experimental results of frequency response

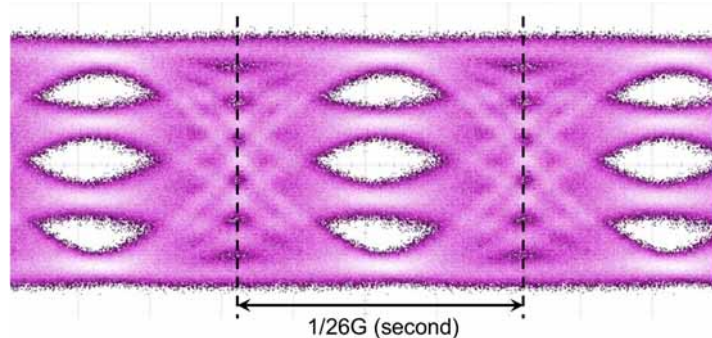


Fig. 3 26Gbaud PAM4 optical eye diagram

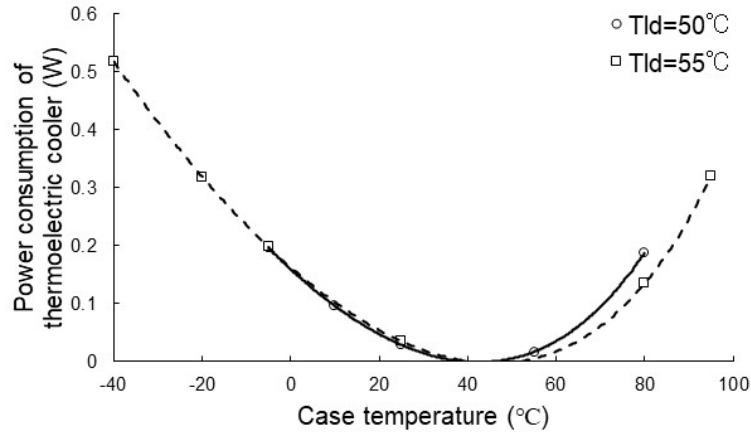


Fig. 4 Experimental results of power consumption of thermoelectric cooler

Table 1 Specifications and experimental results of 50-Gbps EML CAN

Item	Target specification	Evaluation result
Emission wavelength	1,304.5~1,317.5 nm	1,309.1 nm
Optical output(CW)@I _{op} =100mA	≥+10.9 dBm	+12.3 dBm
3dB cutoff frequency	-	19.4 GHz
Extinction ratio	≥6.0 dB	7.0 dB
TDECQ	≤3.2 dB	2.0 dB
Power consumption of thermoelectric cooler	≤0.70 W@-5°C	0.20 W@-5°C
	≤0.42 W@+80°C	0.19 W@+80°C

For the 25-Gbps EML CAN developed for fronthaul, because the service temperature is I-temp (-40 to +95°C), Tld of the EML was determined as 55°C considering the power consumption of the thermoelectric cooler. Meanwhile, because the service temperature of EML CAN for midhaul is C-temp, even if Tld is lowered to increase the EML output, the power consumption of the thermoelectric cooler can be kept low. Therefore, Tld of 50-Gbps EML CAN was determined as 50°C so that the power consumption when the case temperature is -5°C will be at the same level as that when it is +80°C. When I_{op} is 100 mA, setting the temperature to 50°C can increase the optical output by +0.6 dB. Figure 4 shows the power consumption of the thermoelectric cooler when the case temperature was changed from -5°C to +80°C. The power consumption of the thermoelectric cooler was 0.19 W when the case temperature was +80°C and 0.20 W when it was -5°C, which shows that the model can be operated at C-temp.

Table 1 lists the target specifications of the 50-Gbps EML CAN and evaluation results.

6. Conclusion

We have realized 50-Gbps EML CAN that operates with 26-Gbaud PAM4 for midhaul of 5G base stations. The optical waveforms were evaluated and the obtained characteristics conform to standard 50GBASE-ER.

References

- (1) Watanabe, Y., et al.: 25-Gbps Can-type EML for 5G Mobile Base Stations, Mitsubishi Electric ADVANCE Vol. 168 (2019)
- (2) Yamatoya, T., et al.: Novel Hybrid-Waveguide EMLs for 100 Gb/s CFP2 Transceivers, 18th OECC/PS, MK1-2 (2013)

100-Gbps EML CAN for 5G Mobile Communication System

Authors: *Seiji Nakano** and *Masaki Nasu***

1. Introduction

Data traffic is rapidly increasing due to the spread of mobile communication devices and the use of cloud computing systems to exchange information. In response, mobile communication systems are being shifted from 4G to 5G around the world. This requires large-capacity optical communication systems between backbone networks and base stations, driving demand for 100-Gbps products.

In the structure of conventional 25-Gbps electro-absorption modulated laser (EML) CAN, there are many specular points of high-frequency signals due to impedance mismatch, making it difficult to secure the signal passband required for 100-Gbps high-speed operation.⁽¹⁾ Accordingly, we have developed a new structure with a wider signal passband as follows. The band of the EML element was widened, sections related to impedance mismatch in the package structure were reviewed, and a metal plate was introduced between the package and flexible printed circuit (FPC), which has made it possible to reduce signal reflection. In addition, components for 25-Gbps EML CAN were used to reduce the cost and the 4-level pulse amplitude modulation (PAM4) system in which a single pulse signal carries 2-bit data is supported, which has led to 100-Gbps optical signal transmission devices with a communication speed that is four times faster.

2. EML Element Design

In the adopted hybrid structure, a buried-type DFB with excellent high-temperature properties and an EA modulator with a high-mesa waveguide are monolithically integrated.⁽²⁾ For the high-mesa waveguide, the optical confinement rate is high even when the width of the waveguide is narrow and the trade-off relationship between the band and extinction ratio can be eased. In order to realize high-speed operation of 100 Gbps, the band needs to be expanded by reducing the capacitance of the EA modulator and the extinction ratio needs to be secured at the same time. To achieve this, the length of the modulator was made shorter than the conventional model to reduce the capacitance; the extinction ratio, which is in a trade-off relationship, was reduced compared to the conventional model while the 100G Lambda MSA LR1

specifications⁽³⁾ were satisfied in the design.

3. Design to Expand the Band of EML CAN

For operation at 100 Gbps, the passband needs to be 35 GHz or higher in general. The output impedance of the circuit for driving the device is 50Ω. Therefore, optimizing the impedance of the EML CAN structure to 50Ω reduces reflection, which makes it possible to expand the band. However, the impedance mismatch in the conventional CAN structure needs to be reduced.

Figure 1 shows the appearance and internal structure of this product. Usually, an FPC is connected to the rear of the stem to install the product into a transceiver. As the internal structure, the FPC is connected to the EML via the glass penetration section and electrical signals are sent. In the conventional structure, the impedance of the glass penetration section is not 50Ω, which limits the band. Consequently, for this product, the diameter of the signal pin and the permittivity of the glass material were reduced, bringing the impedance close to 50Ω. In addition, the material of the reinforcing plate of the FPC was changed to an electrically conducting material and the reinforcing plate was implemented above the GND layer, which enhanced the GND between the stem and FPC.

4. EML CAN Evaluation Results

Table 1 lists the target specifications of this product and evaluation results. Figure 2 shows a comparison of the frequency response characteristics (S21) between this product and 25-Gbps EML CAN. The figure shows that the -3-dB passband width of 25-Gbps EML CAN is up to 19 GHz while that of this product has been extended up to 36 GHz.

Next, to evaluate the optical waveforms, a digital signal processor (DSP) with an internal driver was used. In the established evaluation system, a data pattern in the 53.125-GBd PAM signal transmission mode (short stress pattern random quaternary (SSPRQ)) was created and input to this product; the PAM4 optical waveforms output from this product were evaluated using a special optical oscilloscope. In the evaluation, the intensity levels of the four values were adjusted so as to minimize the transmitter and dispersion eye closure quaternary (TDECQ), which is the standard for evaluating PAM4 optical waveforms.

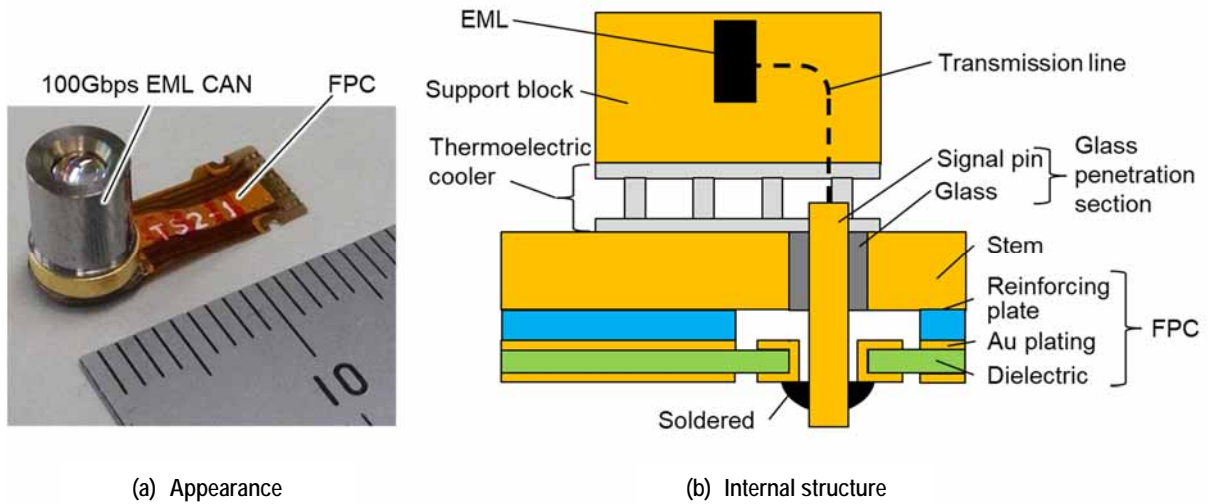


Fig. 1 Appearance and internal structure

Table 1 Product target specifications and evaluation results

Item	Target specification	Evaluation result
Emission wavelength	1304.5~1317.5nm	1312.0nm
Optical output (CW, $I_{op} = 100 \text{ mA}$)	$\geq 10.5 \text{ dBm}$	12.8dBm
Optical modulation amplitude at the time of modulation	0.8~4.6dBm	0.8~4.6dBm ($I_{op} = 60 \sim 80 \text{ mA}$)
-3-dB passband	$\geq 35 \text{ GHz}$	36GHz
Extinction ratio at the time of modulation	$\geq 5.0 \text{ dB}$	5.6dB
TDECQ	$\leq 3.4 \text{ dB}$	2.5dB
Power consumption of thermoelectric cooler	$\leq 0.7 \text{ W} @ -40^\circ\text{C}$ $\leq 0.5 \text{ W} @ 95^\circ\text{C}$	0.46W @ -40°C 0.38W @ 95°C

Figure 3 shows the back-to-back (BTB) PAM4 optical waveforms measured with the oscilloscope. As the evaluation results, the extinction ratio at the time of modulation (outer ER) was 5.6 dB and TDECQ was 2.5 dB; thus, they have margins compared to the LR1 specifications. The evaluation also revealed that the optical modulation amplitude at the time of modulation (outer OMA) also satisfies the LR1 specifications.

Figure 4 shows the power consumption of the thermoelectric cooler when the case temperature (T_c) was changed from -40°C to $+95^\circ\text{C}$. The consumption of this product is similar to that of 25-Gbps EML CAN and the power consumption per Gbps could be reduced to one quarter that of conventional 25-Gbps EML CAN. Regarding the product specifications, the power consumption is 0.7 W when T_c is -40°C and 0.5 W when T_c is 95°C .

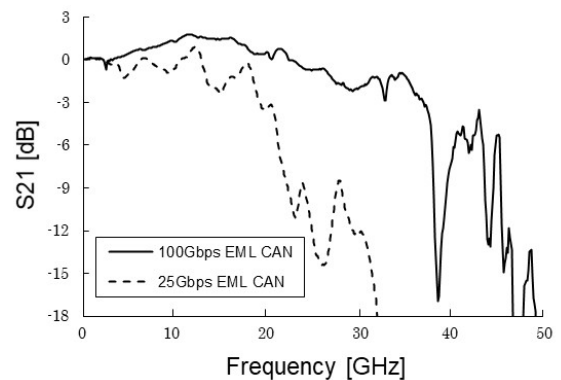


Fig. 2 Frequency response characteristics of this product and 25-Gbps EML CAN (S21)

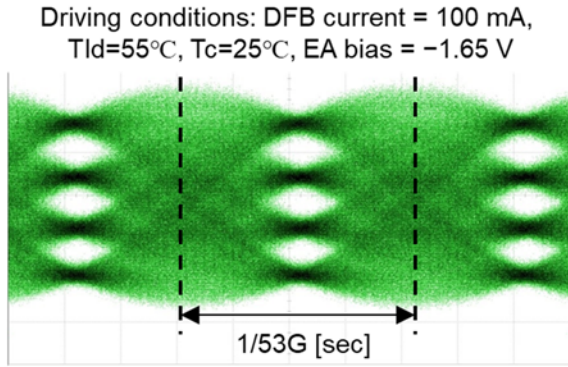


Fig. 3 PAM4 optical waveform

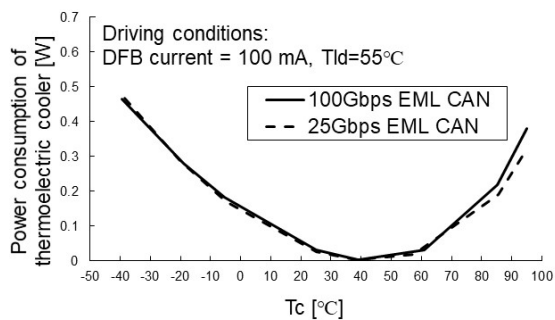


Fig. 4 Evaluation results of power consumption of thermoelectric cooler

5. Conclusion

Mitsubishi Electric has developed 100-Gbps EML CAN for 5G mobile base stations. To expand the band, the length of the EA modulator in the EML element was reduced, the impedance of the stemmed glass penetration section and other sections was matched as the package structure, and an electrically conducting material was used as the reinforcing plate of the FPC. These improvements reduced signal reflection and achieved the passband of 35 GHz or higher. To evaluate the optical waveforms, a DSP with an internal driver was used. The obtained BTB showed that the outer ER was 5.6 dB and TDECQ was 2.5 dB; these values have margins compared to the 100G Lambda MSA LR1 specifications. The power consumption of the thermoelectric cooler was 0.46 W when T_c was -40°C and 0.38 W when it was +95°C. The power consumption per Gbps was reduced to one quarter that of 25-Gbps EML CAN, thus greatly reducing the energy consumption of optical communication systems.

References

- (1) Okada, N., et al.: Cost-Effective 10.7Gbit/s Cooled TOSA Employing Rectangular TO-CAN Package Operating up to 90°C, OFC, JWA38 (2010)
- (2) Morita, Y., et al.: 1.3 μm 28 Gb/s EMLs with Hybrid Waveguide Structure for Low-Power- Consumption CFP2 Transceivers, OFC, America, paper OTh4H.5 (2013)
- (3) 100G LAMBDA MSA, 100G-FR and 100G-LR Technical Specifications Rev 2

80×60 Pixels Thermal Diode Infrared Sensor

Authors: *Yoshinori Takahashi** and *Tomohiro Maegawa**

1. Introduction

In 2019, Mitsubishi Electric Corporation developed MIR8032B1 with 80×32 pixels as a proprietary thermal diode infrared sensor module, MeIDIR, for general consumer use. The number of pixels of this module is approximately ten times and the temperature resolution (100 mK) is approximately five times those of thermopile infrared sensors with 16×16 pixels that are generally used in the market.

This paper describes the technical characteristics of MeIDIR and also the characteristics of MIR8060B1, a new model of the MeIDIR series in which the number of pixels was increased to 80×60.

2. Infrared Sensors

2.1 Characteristics of infrared sensors

Infrared sensors convert the received infrared rays into electrical signals to detect the heat of objects without contact. Although infrared sensors detect the heat of objects, they do not sense visible light and so are characterized by being less affected by module by minute particles, etc. in the air. Figure 1 compares typical infrared and visible images. These images show that

(1) night vision is possible, (2) the influence of ambient light is small, and (3) the influence of scattering is small (e.g., even when the area is filled with smoke, the objects can be identified). In addition, when a human is photographed, although the human body can be recognized based on the heat generation conditions, the person cannot be identified. Therefore, the module is suitable for applications requiring privacy protection.

3. MeIDIR

3.1 Infrared sensor module MeIDIR

Mitsubishi Electric developed new resolution and price range product MeIDIR compared to conventional thermopiles and bolometers using its original thermal diode sensor technology.

3.2 Technology to improve the sensitivity of MeIDIR

Thermal infrared sensors detect temperature changes by absorbing the received infrared rays with temperature detectors. If the thermal conductance between the temperature detector and surrounding environment is high, the detection sensitivity degrades.

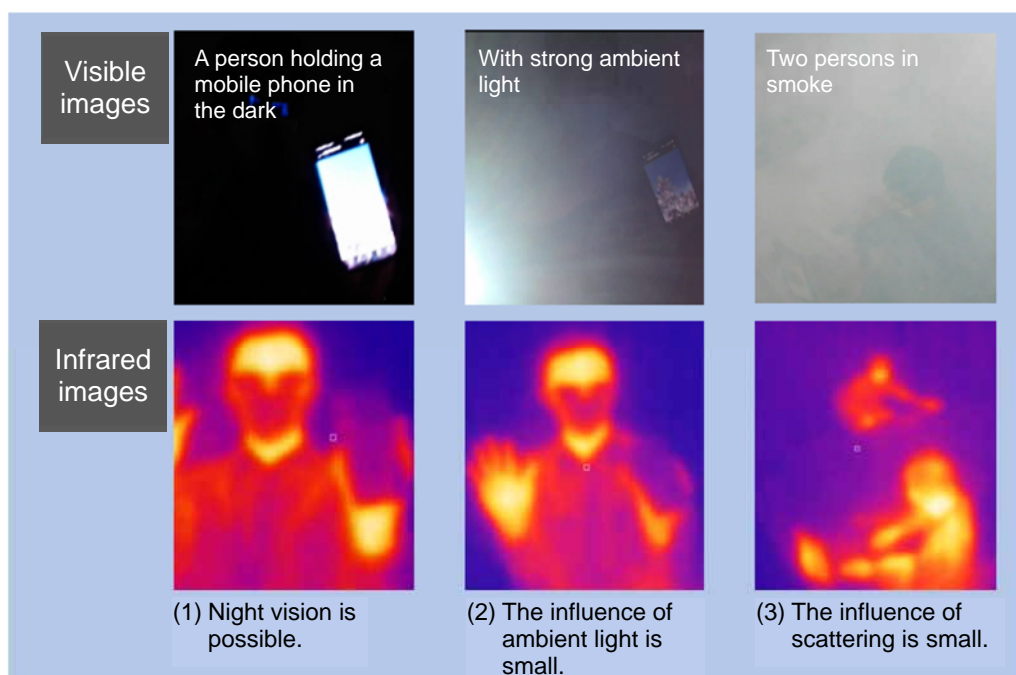


Fig. 1 Features of infrared sensor

To prevent this, for MeDIR, a cavity structure was formed between the diodes (pixels) and silicon substrate, which is the base material used to form the element (Fig. 2), and chip-scale packaging technology for directly mounting sealing window parts onto the sensor chip (Fig. 3) was used to maintain a vacuum inside the package, thus ensuring high sensitivity.

3.3 Technologies for the small module

In addition to a sensor element that detects infrared rays, an infrared sensor requires an optical system that gathers infrared rays emitted from a distant place to the temperature detector, a control function for driving the sensor element, and a function for converting the voltage that the temperature detector converted from the heat through thermoelectric conversion and output into digital signals.

MeDIR module consists of a silicon lens that gathers infrared rays to the sensor temperature detector, a sensor IC that detects infrared rays, a thermistor that measures the temperature of the module and an

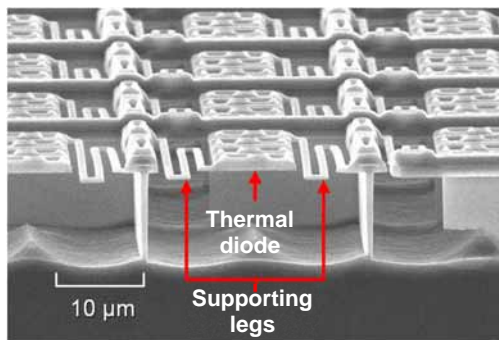


Fig. 2 Enlarged photo of temperature detector

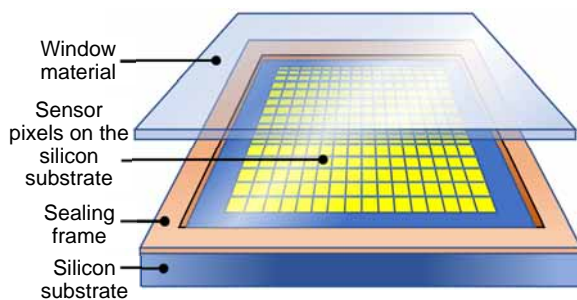


Fig. 3 Structural drawing of chip-scale vacuum package

application-specific integrated circuit (ASIC) that contains sensor control, signal processing, and MCU communication functions. The ASIC also has a one-time programmable read-only memory (OTP ROM) to which various parameters are saved as factory settings, in addition to the main control functions. Information specific to each module can be stored in the OPT ROM before it is shipped.

Figure 4 shows the appearance of MeDIR. The thermal diode sensor and ASIC developed for MeDIR have been mounted inside the lens cap of the silicon lens. On the rear of the sensor are mounted a thermistor that measures the temperature of the module, a connector for exchanging signals with the outside of the sensor, and other surface mount devices.

4. Sensor MIR8060B1 with 80×60 Pixels

4.1 Characteristics of MIR8060B1

Although the shape of MIR8060B1 is the same as that of the conventional MIR8032B1, the angle of view was expanded to approximately 1.8 times and the number of pixels was increased to approximately 1.9 times. The new product can detect an area two to four times larger than the conventional product even under the same installation conditions. The increase in number of pixels and wider angle of view have made it possible to recognize heat objects and understand their behavior in a wide area. In addition, the new product has a function for switching to eight frames per second (fps) in addition to the conventional four fps, delivering higher performance for detecting moving heat objects.

A camera and the two types of sensors were installed on the ceiling (approximately 2.5-m high) of a general office building. Figure 5 shows a visible image of the corridor and thermal images in the angle of view of MIR8032B1 and in the angle of view of MIR8060B1.

In the angle of view of MIR8032B1, the person at the end of the corridor is outside the angle of view and so cannot be clearly recognized. Meanwhile, in the MIR8060B1 image, the person at the end can be clearly seen.

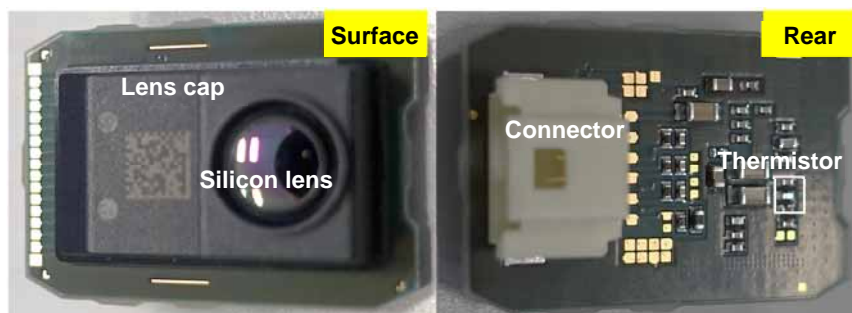


Fig. 4 Exterior photo of MeDIR

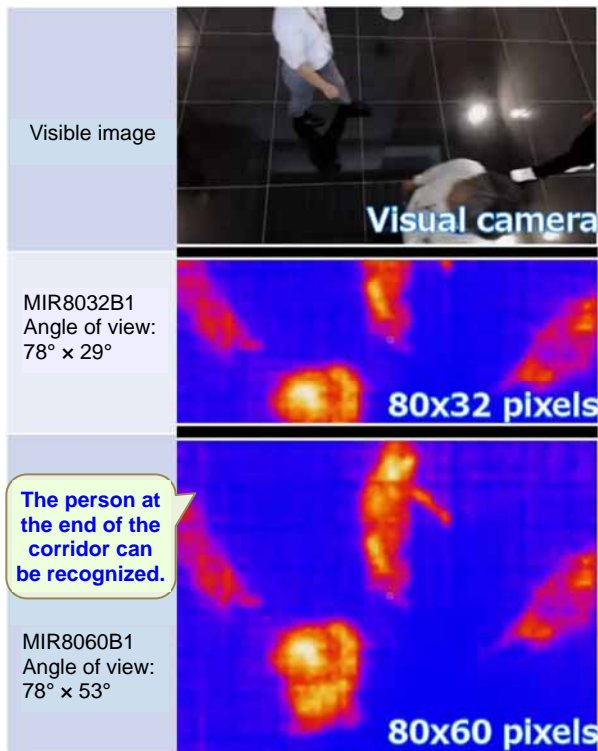


Fig. 5 Image comparison by angle of view

for detecting moving heat objects, in addition to the conventional markets of air conditioning and body surface temperature measurement, thus contributing to society.

4.2 User support tool

Regarding MeDIR, since launching sales of MIR8032B1, we have been expanding the tool for supporting evaluation and development by customers. For MIR8060B1, the tool started to be provided at the same time as the release of the product.

The user support tool includes a document suggesting various ways to use MeDIR assuming various applications by customers, a thermal image library containing actual scene images, a microcomputer kit for evaluation that can be used to evaluate the product, reference codes for supporting software and hardware design in users' product development, and a reference design.

5. Conclusion

Mitsubishi Electric has developed the infrared sensor module MeDIR for markets where conventional infrared sensors are unsuitable. In addition to the 80×32-pixel MIR8032B1 which went on sale in 2019, we developed, in 2021, the new MIR8060B1 to increase our product types. Although MIR8060B1 has the same shape as MIR8032B1, the number of pixels was increased to 80×60 pixels to make it possible to sense wider area, and eight fps was added as the frame rate in addition to the conventional four fps, enabling switching. This improved performance expands applications in new markets, such as crime prevention, monitoring, person counting, and smart buildings, by leveraging the wider angle of view and the performance

Shortening of Evaluation Time by Highly Accelerated Stress Test and Improvement of Analysis Technique for Passivation Film

Authors: Koichi Inoue* and Hajime Sasaki*

1. Introduction

Optical semiconductor devices are often put in hermetic packages to prevent the characteristics from changing depending on the temperature and humidity of the environment. However, because more devices have been used without hermetic packages in recent years for some applications, it has become essential to secure and verify the humidity robustness of the devices themselves. As reliability standards for optical semiconductor devices, Telcordia GR-468-CORE issue 2⁽¹⁾ is often used. A high temperature and high humidity test under temperature and humidity conditions conforming to the standards (85°C/85%RH) takes several thousand hours, which can cause problems for product development schedules. In order to study changes in characteristics that occur in products on the market, this test time needs to be reduced. In evaluating the humidity robustness of optical semiconductor devices under development, we studied whether highly accelerated stress tests could be applied, and report the results here.

2. Application of HAST Conditions and Acceleration

We considered applying highly accelerated stress tests (HAST) as further accelerated tests in place of high temperature and high humidity tests at 85°C/85%RH conforming to the specifications of Telcordia GR-468-CORE issue 2. When HAST is introduced, it is important to note that if a phenomenon different from the change mechanism in the original service environment appears, the test is not regarded as an accelerated test.

As the temperature and humidity conditions of this HAST, the temperatures were determined as 115°C and 130°C (two conditions) and the humidity was determined as 85%RH (single condition). Table 1 lists the absolute water vapor pressure for the temperature and humidity environments. The table shows that the higher the temperature is, the higher the absolute water vapor pressure is.

Figure 1 is a schematic diagram of a HAST chamber. The steam generated by heating the water is further heated; a fan is used for mixing and a valve is used to

adjust the pressure to create a high temperature and high humidity environment in the single-chamber tester used. Figure 2 is a graph showing the duration of the high temperature and high humidity test until the

Table 1 Absolute water vapor pressure versus high temperature and high humidity conditions

Temperature and humidity conditions	Absolute water vapor pressure (kPa)
55°C/85%RH	13.3
65°C/85%RH	21.3
85°C/85%RH	49.1
115°C/85%RH	143.0
130°C/85%RH	229.0

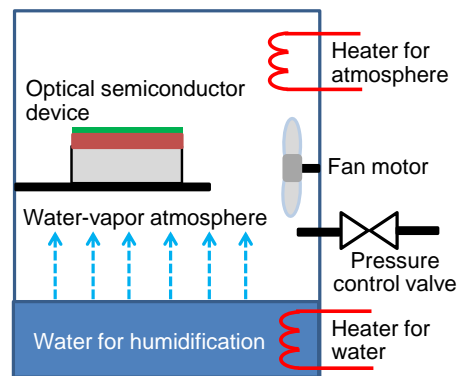


Fig. 1 Schematic drawing of HAST chamber

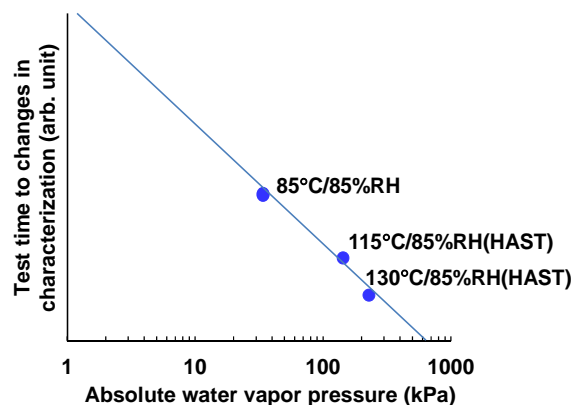


Fig. 2 Duration of high temperature and high humidity test for changes in characteristics versus absolute water vapor pressure

characteristics of the optical semiconductor devices changed to the absolute water vapor pressure. The evaluation was made for a total of three conditions including the results of a test at 85°C/85%RH conforming to Telcordia GR-468-CORE issue 2. As a result, when the test time until the characteristics changed was plotted against a power of the absolute water vapor pressure, a correlation was found.

3. Analysis Techniques Used after the Test and Analysis Results

3.1 Analysis techniques used after the test

The results of the high temperature and high humidity test indicate that under the HAST conditions, acceleration was obtained. In order to judge whether the result is appropriate, the optical semiconductor device before and after the test needs to be analyzed to confirm that the change mechanism is the same as that under conventional test conditions.

The results of reliability tests obtained in the past show that changes in moisture absorption by silicon nitride films, which are used to protect the surfaces of optical semiconductor devices, cause deterioration. Accordingly, we focused on the silicon nitride film for comparison. As the check methods, a scanning transmission electron microscope (STEM) was used for observation, and energy dispersive X-ray spectroscopy (EDX) and electron energy loss spectroscopy (EELS) were used to analyze the composition and evaluate the chemical bonding state. Figure 3 illustrates the configuration of the measurement system consisting of STEM, EDX, and EELS.

3.2 Analysis by STEM, EDX, and EELS

The silicon nitride film before and after the high temperature and high humidity test was observed with STEM and analyzed by EDX mapping, and the results were compared. Figure 4 shows the oxygen (element) mapping results. The figure shows that on the surface of the silicon nitride film on the top layer of the optical semiconductor device, the contrast in the STEM images after the tests is different from that before the test and oxygen was detected on the sections.

The EDX analysis results clearly show that oxygen exists on the surface of the silicon nitride film after the high temperature and high humidity test. In order to inspect the composition and chemical bonding state at the section more closely, EELS analysis was performed. Figure 5 shows an enlarged STEM image of the silicon nitride film after the high temperature and high humidity test (130°C/85%RH) along with points analyzed by EELS. Figure 6 shows the STEM-EELS spectra by point analysis. The analyzed points were points 1 and 2 in Fig. 5. At point 2, which is located more than 4 nm inside

from the surface, there is silicon nitride.⁽²⁾⁽³⁾ Near 106 eV, there is a peak due to absorption by the L2 and L3 shells and near 160 eV, there is a peak due to absorption by the L1 shell. 106 eV is by the Si-N bond. On the other hand, at point 1, which is located approximately 2 to 3 nm from the surface, there is silicon oxide.⁽²⁾⁽³⁾ Near 108 eV and 116 eV, there are peaks by absorption by the L2 and L3 shells and near 160 eV, there is a peak by absorption by the L1 shell. These results show that the area approximately 2 to 3 nm from the surface of the silicon nitride film reacted with oxygen to form silicon oxide and volume expansion occurred; as a result, the stress applied to the optical semiconductor device

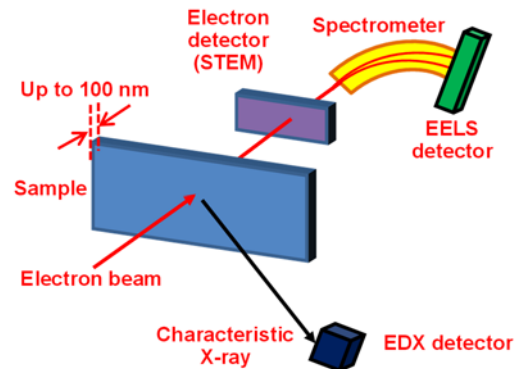


Fig. 3 Configuration of STEM, EDX and EELS

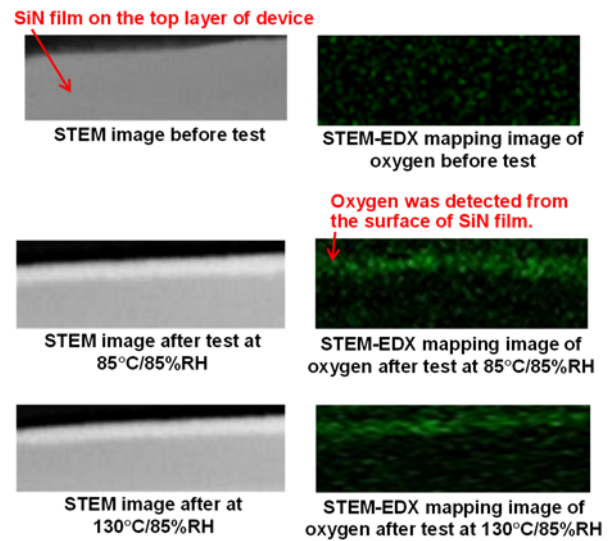


Fig. 4 STEM images and oxygen mappings by EDX

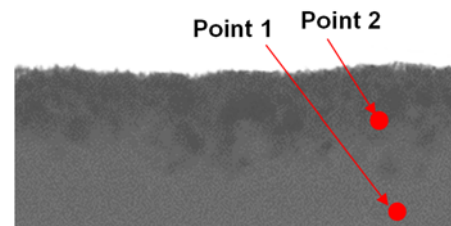


Fig. 5 EELS analysis points on silicon nitride film after test at 130°C/85%RH

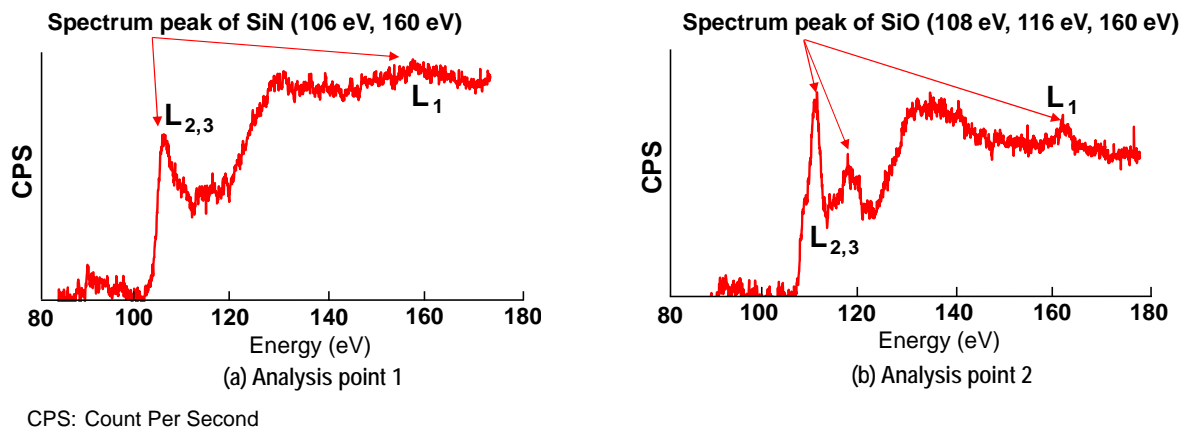


Fig. 6 EELS energy spectrum on silicon nitride film after test at 130°C/85%RH

changed, which caused the changes in characteristics. These changes were the same for the high temperature and high humidity tests at 130°C/85%RH (HAST conditions) and at 85°C/85%RH.

These results show that highly accelerated stress tests can be applied. This will greatly contribute to verifying the humidity robustness of products under development more efficiently in the future.

4. Conclusion

We studied whether highly accelerated stress tests could be used to evaluate the humidity robustness of optical semiconductor devices under development. The results showed that the change mechanism of the optical semiconductor devices is the same between the high temperature and high humidity tests at 130°C/85%RH and at 85°C/85%RH conforming to Telcordia GR-468-CORE issue 2. This finding demonstrates that the highly accelerated stress test can be applied as an appropriate test procedure. Reducing the duration of the high temperature and high humidity test using these conditions will shorten the time required for reliability tests in product development.

References

- (1) Telcordia: Generic Reliability Assurance Requirements for Optoelectronic Devices Used in Telecommunications Equipment, GR-468 Issue Number 02 (2004)
- (2) Maigne, A., et al.: Review of recent advances in spectrum imaging and its extension to reciprocal space, *J. Electron Microscopy*, 1 (2009)
- (3) Park, J., et al.: Electron Energy Loss Spectroscopy Characterization of TANOS (TaN/Al₂O₃/Si₃N₄/SiO₂/Si) Stacks, *Microsc Micronal*, 19, S5, 109 (2013)

